L'effet de la taille et du fluide actif sur la conception multi-objectifs des compresseurs centrifuges à grande vitesse

Giuffre, Andrea; Colonna, Piero; Pini, Matteo

DOI
10.1016/j.ijrefrig.2022.06.023

Publication date
2022

Document Version
Final published version

Published in
International Journal of Refrigeration

International Journal of Refrigeration 143 (2022) 43–56

Contents lists available at ScienceDirect

International Journal of Refrigeration

journal homepage: www.elsevier.com/locate/ijrefrig

The Effect of Size and Working Fluid on the Multi-Objective Design of High-Speed Centrifugal Compressors

L'effet de la taille et du fluide actif sur la conception multi-objectifs des compresseurs centrifuges à grande vitesse

Andrea Giuffre, Piero Colonna, Matteo Pini *

Propulsion and Power, Delft University of Technology, Kluyverweg 1, Delft, 2629HS, The Netherlands

ARTICLE INFO

Keywords:
Heat pumps
Working fluids
Centrifugal compressors
Multi-objective optimization
Environmental control system (ECS)
Computational fluid dynamics (CFD)
Mots clés:
Pompes à chaleur
Fluides actifs
Compresseurs centrifuges
Optimisation à objectifs multiples
Système de contrôle environnemental (ECS)
Mécanique numérique des fluides (CFD)

ABSTRACT

The impact of size and working fluid on the efficiency, operating range, and axial thrust on bearings is examined for high-speed, oil-free centrifugal compressors. First, the development and validation of a reduced-order model based on scaling principles is documented. Then, the validated compressor model is used to generate design maps for stages operating with arbitrary fluid molecules, and characterized by different size. The results show that compressors operating with fluids made by heavy and complex molecules provide lower efficiency over the entire design space, if compared to their simple-molecule counterparts. However, compressors for complex-molecule fluids require lower rotational speed, and generate lower axial thrust on bearings, thus making them particularly suitable for small-scale applications. Furthermore, a decreasing value of the size parameter has a detrimental effect on the stage efficiency, as a result of manufacturing constraints. The results computed by the compressor model suggest that the efficiency penalty is more sensitive to variations of clearance gap than to surface finishing. Lastly, the reduced-order model has been used to perform a design exercise, i.e., the multi-objective optimization of the first compressor stage of the heat pump test rig being realized at Delft University of Technology. The key characteristics of the optimal compressor design has been compared to those derived from the design maps, to corroborate their validity. The optimal design has been extensively characterized by means of CFD, providing further evidence that efficient mini-compressors operating with organic fluids, and featuring pressure ratios up to five at off-design, are feasible.

1. Introduction

The recent advancements in the field of high-speed permanent magnet electric motors (Zwyssig et al., 2009) have triggered the development of miniature high-speed centrifugal compressors, i.e., machines featuring an impeller tip diameter as small as 30 mm, and a rotational speed as high as 200 krpm. The possible applications of this technology include heat pumps (Schiffmann and Favrat, 2009), mini gas turbines (Pilavachi, 2002), cryogenic coolers based on the inverse Brayton cycle (Zagarola and McCormick, 2006), fuel cell air management systems, and electrical supercharging (Casey et al., 2013). Schiffmann et al. recently demonstrated the technical feasibility of an efficient small-scale centrifugal compressor for domestic heat pump applications (Schiffmann and Favrat, 2009; 2010). The adoption of an electrically-driven heat pump, featuring a high-speed centrifugal compressor, for the environmental control system (ECS) of next-generation aircraft is currently under investigation at Delft University of Technology. The ECS is the main secondary power consumer on board of aircraft, accounting for $\approx 75\%$ of non-propulsive power, i.e., up to $3-5\%$ of the total energy consumption (Bender, 2018). The use of electric power in place of engine-generated pneumatic power can lead to fuel savings in the range of $1-2\%$ for medium-long haul aircraft at cruise conditions (Boeing, 2007). Moreover, the replacement of the traditional air cycle machine (ACM), i.e., an inverse Brayton cycle, with a more efficient vapor compression cycle (VCC) system can promote a

Abbreviations: CO_2, Carbon dioxide; ECS, Environmental control system; H_2, Hydrogen; IRIS, Inverse Rankine integrated system; R1233zd(E), Trifluoropropene; R134a, Tetrafluoroethane.

* Corresponding author. Tel.: (+31)152784794.
E-mail addresses: a.giuffre@tudelft.nl (A. Giuffre), p.colonna@tudelft.nl (P. Colonna), m.pini@tudelft.nl (M. Pini).

https://doi.org/10.1016/j.ijrefrig.2022.06.023
Received 19 January 2022; Received in revised form 17 June 2022; Accepted 19 June 2022
Available online 20 June 2022

Nomenclature

Roman symbols

A	Surface area [m^2]
a	Sound speed [ms^{-1}] - throat length [m]
c	Specific heat capacity [J kg^{-1} K^{-1}]
C_f	Skin friction coefficient [-]
D	Diameter [m]
F_{ax}	Axial thrust acting on bearings [N]
F_0	Slip factor coefficient [-]
H	Blade height [m]
H^*	Sudden expansion coefficient [-]
h	Specific enthalpy [J kg^{-1}]
i	Incidence angle [deg]
k	Impeller shape factor [-] - empirical constant [-]
L_{ax}	Impeller axial length [m]
M	Mach number [-]
$\dot{m}$	Mass flow rate [kg s^{-1}]
N_{bl}	Number of main blades [-]
N_{split}	Number of splitter blades [-]
N_{eff}	Effective number of blades [-]
N_s	Specific speed [-]
OR	Operating range [-]
P	Pressure [Pa
Pr	Prandtl number [-]
R	Radius [m] - specific gas constant [J kg^{-1} K^{-1}]
Ra	Surface roughness [m]
Re	Reynolds number [-]
SP	Size parameter [-]
s	Specific entropy [J kg^{-1} K^{-1}]
T	Temperature [K]
t	Thickness [m]
U	Peripheral speed [ms^{-1}]
V	Absolute velocity [ms^{-1}]
$\dot{V}$	Volumetric flow rate [m^3s^{-1}]
v	Specific volume [m^3K^{-1}]
W	Relative velocity [ms^{-1}]
w_{eul}	Euler work [J kg^{-1}]

Greek symbols

α	Absolute flow angle [deg]
β	Pressure ratio [-] - relative flow angle [deg]
γ	Heat capacity ratio [J kg^{-1} K^{-1}]
γ_{Pv}	Isentropic pressure-volume exponent [J kg^{-1} K^{-1}]
ϵ_b	Back face clearance [m]
ϵ_t	Tip clearance gap [m]
ϵ_w	Wake area fraction [-]
η	Efficiency [-]
μ	Dynamic viscosity [Pa s^{-1}]
ρ	Density [kg m^{-3}]
$\boldsymbol{\sigma}$	Stage geometrical characteristics [-]
Φ_{t1}	Swallowing capacity [-]
χ	Degree of reaction [-] - Diffuser inclination [deg]
ψ	Work coefficient [-]
Ω	Rotational speed [rpm]
ω	Turbulence specific dissipation rate [s^{-1}]
κ	Turbulence kinetic energy [J kg^{-1}]

Subscripts

a	Throat section
c	Critical
choke	Choking point
cn	Cone
h	Hub
hd	Hydraulic
is	Isentropic
le	Leading edge
r	Reduced
s	Specific - shroud
t	Total - turbulent
te	Trailing edge
ts	Total-to-static
tt	Total-to-total
θ	Tangential component
des	Design point
m	Meridional component
mx	Mixing
rc	Recirculation
sf	Skin friction
sw	Shock waves
i	Incidence
bl	Blade loading
cl	Clearance
vl	Volute
vd	Vaneless diffuser
df	Disk friction
lk	Leakage
1	Inducer
2	Exducer - diffuser inlet
3	Diffuser outlet - volute inlet
4	Volute outlet - cone inlet
P	Evaluated at constant pressure
v	Evaluated at constant volume
2	
2	

further step increase of coefficient of performance (COP). The main drivers for the use of high-speed centrifugal compressors in place of standard volumetric machines for airborne heat pumps are: i) the potential for reaching higher compressor efficiency, thus higher COP; ii) the overall volume and weight reduction; iii) the absence of lubricant oil in the circuit, due to the adoption of foil bearings (Heshmat et al., 2000).

The requirements for the optimal design of mini centrifugal compressors are high efficiency, wide operating range, and high power density. On top of that, the design must comply with strict constraints on the minimum impeller dimensions for manufacturability, on the maximum allowable rotational speed, and on the maximum tolerable axial thrust, to enable the use of gas bearings. As demonstrated by Casey et al. (2013), halving the impeller outlet diameter, while keeping the mass flow rate constant, i.e., shifting towards an impeller design featuring a larger swallowing capacity

$$\Phi_{t1} = \frac{\dot{m}}{\rho_{t1} U_2 D_2^2}, \tag{1}$$

leads to an increase of power density by a factor of eight. More compact stages entail lower material and machining cost, lower weight and inertia, a smaller frontal area, thus a lower axial thrust. In contrast, a reduction of the impeller outlet diameter at constant work coefficient

$$\psi = \frac{\Delta h_{tt}}{U_2^2}, \tag{2}$$

can lead to an increase of rotational speed up to the mechanical limits of the impeller material. Moreover, compressor downsizing comes at the expense of larger friction and clearance losses, due to the increase of relative surface roughness and relative clearance at blade tip.

The selection of the optimal compressor design parameters is further complicated by the choice of the working fluid, which, in turn, is dictated by the design requirements of the heat pump. As an illustrative example, consider two stages providing the same total-to-total pressure ratio $\beta_{tt} = 3$, but operating with two different fluids: hydrogen and refrigerant R134a. The isentropic pressure-volume exponent (Kouremenos and Kakatsios, 1985)

$$\gamma_{Pv} = -\frac{v}{P}\frac{\partial P}{\partial v}\Big|_s = -\frac{v}{P}\frac{c_p}{c_v}\frac{\partial P}{\partial v}\Big|_T, \tag{3}$$

can be used to express the isentropic work performed by a compressor stage operating with an arbitrary working fluid as

$$\Delta h_{tt,is} = \frac{a_{t1}^2}{\gamma_{Pv}-1}\left(\beta_{tt}^{\frac{\gamma_{Pv}-1}{\gamma_{Pv}}} - 1\right). \tag{4}$$

By combining Eqn. (3) and Eqn. (2), the impeller tip speed Mach number $M_{U_2} = U_2/a_{t1}$ can be correlated to the pressure ratio of the stage as

$$M_{U_2} = \sqrt{\frac{\beta_{tt}^{\frac{\gamma_{Pv}-1}{\gamma_{Pv}}} - 1}{\psi(\gamma_{Pv}-1)}}. \tag{5}$$

Assuming that both compressor stages are designed at $\psi = 0.8$ and operate at the total inlet conditions specified in Tab. 1, the ratio of the peripheral speed at impeller outlet for the two fluids reads

$$\begin{aligned} \frac{M_{U_2,H_2}}{M_{U_2,R134a}} &= \frac{1.048}{1.147} = 0.91 \\ \frac{U_{2,H_2}}{U_{2,R134a}} &= \frac{M_{U_2,H_2}}{M_{U_2,R134a}}\frac{a_{t1,H_2}}{a_{t1,R134a}} = 5.11. \end{aligned} \tag{6}$$

As consequence, the stage operating with hydrogen must be designed with a higher work coefficient, in order to keep the outlet peripheral speed below an acceptable threshold, therefore penalizing fluid dynamic performance.

2. Objective

The typical procedure for the preliminary design of centrifugal compressors is described in Came and Robinson (1998); Japikse (1996); Van den Braembussche (2019); Whitfield and Baines (1990). A thorough attempt to devise design guidelines for large-scale centrifugal compressors operating with air and featuring vaned diffusers can be found in Rusch and Casey (2013). Extensive studies on similarity parameters used to characterize the off-design performance of compressors operating with non-ideal flows are documented in (Jeong et al., 2020; Pham et al., 2016). The main implications related to the design of small-scale impellers featuring vaneless diffusers are qualitatively described in Javed et al. (2016). However, the aforementioned study is application-specific and, as such, it does not provide generic design guidelines valid for compressors of different scales and operating with arbitrary working fluids. The study documented here aims to bridge this knowledge gap by extending the work of Rusch and Casey (2013). The objective is to develop design maps for single stage compressors, accounting for the influence of the fluid and of the machine size on stage efficiency, operating range, and the magnitude of the axial thrust on bearings. In particular, the influence of the fluid is related to both its molecular complexity and to the thermodynamic conditions of the compression process, that may entail the flow to depart from the ideal gas behavior (Giuffre' and Pini, 2021). The applications in which the effect of flow non-ideality is relevant are arguably limited to compressors for high-temperature heat pumps and supercritical CO_2 cycles for power generation and refrigeration. Within the scope of the present work, only the influence of the fluid molecular complexity is investigated. The design maps are generated by means of an in-house reduced-order model based on scaling principles, and validated with experimental data of reference impellers (Eckardt, 1975; 1976; Japikse, 1987; Schiffmann and Favrat, 2010).

Moreover, the reduced-order model is used to perform a design exercise, i.e., the multi-objective optimization of the first compressor stage to be installed in the heat pump test rig currently under construction at Delft University of Technology, see Fig. 1. The case study features a Pareto analysis, and a complete characterization of the fluid dynamic performance of the optimal design by means of CFD. To corroborate the validity of the proposed design guidelines, the key design variables selected by the optimizer, and the corresponding compressor performance metrics, are compared to the ones that can be derived from the design maps.

3. Methodology

3.1. Conceptual Design based on Scaling Analysis

The main dimensions and performance metrics of a centrifugal compressor stage can be expressed as

$$\boldsymbol{y} = f(\Phi_{t1}, \psi, \alpha_2, \beta, \overline{\gamma_{Pv}}, Re, \boldsymbol{\sigma}), \tag{7}$$

where $\boldsymbol{y}$ is a vector collecting the compressor characteristics and performance metrics. Several considerations can be drawn from Eqn. (7). The impeller flow angles are univocally determined by the swallowing capacity Φ_{t1}, the work coefficient ψ_{is}, and the degree of reaction χ. Here, the degree of reaction is replaced by the absolute flow angle at the inlet of the diffuser α_2, i.e., a parameter directly related to diffuser stability. The work provided by the impeller scales with the pressure ratio β and the thermodynamic behavior of the fluid, determined by the

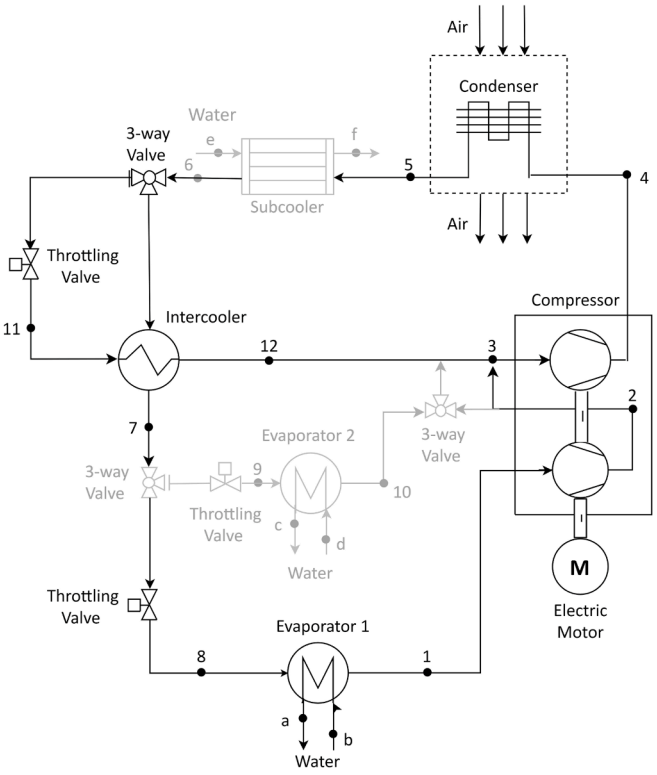

Fig. 1. Simplified P&ID of the IRIS facility currently under construction at Delft University of Technology. The shaded components will be integrated in a second phase.

average value of γ_{Pv} along the prescribed transformation (Giuffre' and Pini, 2021). The impact of the viscous effects is quantified by the average value of the Reynolds number within the impeller, diffuser, and volute. The vector $\boldsymbol{\sigma}$ contains basic information regarding the stage geometry, see Tab. 2. Few of the quantities composing $\boldsymbol{\sigma}$ are intentionally taken as dimensional parameters, because, when dealing with miniature turbomachinery, some geometrical features cannot be scaled due to limits of manufacturability. In Section 4.2 the effect of scale is investigated, by comparing compressor designs characterized by different dimensions, quantified by the value of the size parameter

$$SP = \frac{\dot{V}_1^{1/2}}{\Delta h_{ts}^{1/4}}, \tag{8}$$

but featuring the same values of tip clearance and surface roughness.

The in-house reduced-order model relies on the lumped parameters approach. The flow quantities and the main dimensions of the machine are evaluated at each stream-wise station depicted in Fig. 2. The incoming flow is assumed to be axial and uniform, due to the absence of inlet guide vanes. At the impeller inlet, the flow quantities are evaluated at five different span-wise locations, to capture the free-vortex flow distribution. The relative flow angle at impeller shroud is selected to minimize the local relative Mach number, following the methodology proposed by Rusch and Casey (2013). The effective blade count is defined as $N_{eff} = N_{bl} + 0.75N_{split}$. Splitter blades are considered in the calculations whenever the estimated throat length is smaller than a user-defined threshold, to ensure impeller manufacturability. The diffuser is assumed to be vaneless and pinched close to the inlet section, to delay rotating stall inception. Slip at impeller outlet is accounted for by means of the semi-analytical model of von Backström (2006). Within this model, the value of the empirical constant F_0 has to be tuned for each family of impellers. The external volute is designed resorting to the conservation equations, assuming no friction and no pressure gradient in the circumferential direction, as suggested in Casey and Robinson (2021). The thermo-physical fluid properties are evaluated by means of the reference thermodynamic library developed by NIST (Lemmon et al., 2018). The axial thrust acting on gas bearings is estimated with the method reported in Tiainen et al. (2021)

$$F_{ax} = F_{in} + F_{imp} + F_s - F_{bd}, \tag{9}$$

where F_{in} and F_{imp} are the pressure and the impulse forces acting on impeller inlet, whereas F_s and F_{bd} refer to pressure forces acting on the shroud and the back disk, respectively. Within this model, the shaft is assumed to be of the cantilever type, and the impeller is assumed to have no radial labyrinth seals. The shaft radius is either an input from the user, or is expressed as a fraction of the impeller hub radius. The design maps presented in the following section were obtained by assuming a given fraction of the impeller hub radius, to preserve the effect of scaling.

3.2. Loss Modeling

The compressor efficiency is evaluated as a function of the internal and external loss sources, expressed in terms of total enthalpy loss, namely

$$\eta_{tt} = \frac{w_{eul} - \Delta h_{t,int}}{w_{eul} + \Delta h_{t,ext}}. \tag{10}$$

The internal losses affect both the pressure ratio and the stage efficiency. The loss mechanisms that are not associated to the main flow are grouped in the so-called parasitic or external losses. They affect the stage efficiency, but they have no influence on the pressure ratio.

If the flow at the inlet of the impeller is supersonic, the entropy production associated to the presence of shock waves is accounted for by means of the model proposed by Denton (Denton, 1993), extended to non-ideal flows, i.e.,

$$\Delta s_{sw} = c_{v,1} \frac{2\overline{\gamma_{pv}}\left(\overline{\gamma_{pv}} - 1\right)}{3\left(\overline{\gamma_{pv}} + 1\right)^2} \left(M_{W1}^2 - 1\right)^3. \tag{11}$$

At off-design conditions, the incidence angle deviates from the estimated

Table 1
Fluid properties and total inlet conditions specified in the reduced-order model to create the design maps.

Fluid	P_{t1} [bar]	T_{t1} [K]	$R\left[\frac{J}{kg \cdot K}\right]$	$\overline{\gamma_{Pv}}$
Argon	2.0	253.15	208.13	1.674
H_2	1.2	103.15	4124.44	1.516
Air	2.5	308.15	287.05	1.402
CO_2	1.5	283.15	188.92	1.271
R134a	0.55	243.15	81.49	1.095
R1233zd(E)	0.5	283.15	63.71	1.055

Table 2
Specification of the compressor geometrical characteristics used in the reduced-order model, and collected in the vector $\boldsymbol{\sigma}$. The values are referred to the design maps presented in Section 4.

Description	Definition	Value
Impeller shape factor	$k = 1 - \left(\frac{R_{1,h}}{R_{1,s}}\right)^2$	0.9
Number of blades	$N_{bl} + N_{split}$	14
Diffuser radius ratio	R_3/R_2	1.5
Diffuser blade height ratio	H_3/H_2	0.85
Diffuser pinch radius ratio	R_{pinch}/R_2	1.3
Non-dimensional length	L_{ax}/R_2	0.7
Leading edge thickness	t_{le} [mm]	2-1-0.2
Trailing edge thickness	t_{te} [mm]	2-1-0.2
Impeller tip clearance	ϵ_t [mm]	0.15
Back face clearance	ϵ_b [mm]	0.15
Surface roughness	Ra [mm]	0.01

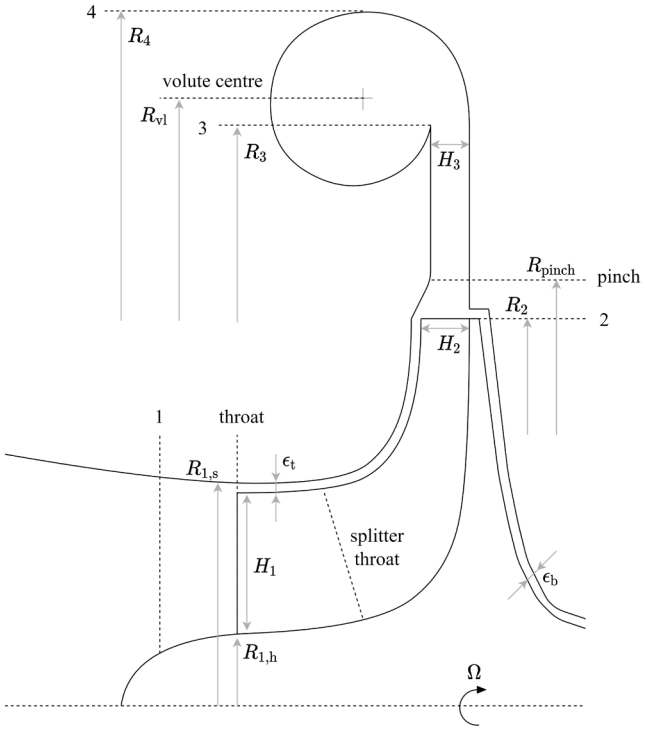

Fig. 2. Meridional view of a centrifugal compressor stage featuring splitter blades, pinched vaneless diffuser, overhung volute, and no inlet guide vanes.

optimal value (Van den Braembussche, 2019), and the associated efficiency loss is computed as (Galvas, 1973)

$$\Delta h_{\mathrm{t,i}} = \frac{\left(W_1 \sin\left|i - i_{\mathrm{opt}}\right|\right)^2}{2}. \tag{12}$$

The impact of viscous friction on the impeller performance is evaluated by means of the model of Jansen (1970)

$$\begin{aligned} \Delta h_{\mathrm{t,sf}} &= 2C_{\mathrm{f}}\frac{L_{\mathrm{hd}}}{D_{\mathrm{hd}}}\overline{W}^2 \\ \overline{W} &= \frac{V_{1,\mathrm{s}} + V_2 + W_{1,\mathrm{s}} + 2W_{1,\mathrm{h}} + 3W_2}{8}, \end{aligned} \tag{13}$$

where the skin friction coefficient is computed according to the weighted average method proposed by Aungier (2000). The losses associated to diffusion in the blade passage are estimated as (Coppage et al., 1956)

$$\begin{aligned} \Delta h_{\mathrm{t,bl}} &= 0.05\cdot\left(D_{\mathrm{f}}U_2\right)^2 \\ D_{\mathrm{f}} &= 1 - \frac{W_2}{W_{1,\mathrm{s}}} + \frac{0.75\dfrac{\left|\Delta h_{\mathrm{tt}}\right|}{U_2^2}\dfrac{W_2}{W_{1,\mathrm{s}}}}{\dfrac{N_{\mathrm{eff}}}{\pi}\left(1 - \dfrac{D_{1,\mathrm{s}}}{D_2}\right) + 2\dfrac{D_{1,\mathrm{s}}}{D_2}}. \end{aligned} \tag{14}$$

The total enthalpy loss due to tip clearance is calculated by means of the correlation introduced by Brasz (1988)

$$\begin{aligned} \Delta h_{\mathrm{t,cl}} &= \frac{0.6\epsilon_t\left|V_{\theta,2}\right|}{H_2 + \dfrac{\epsilon_t}{2}}\sqrt{\frac{4\pi\left|V_{\theta,2}\right|V_{\mathrm{m},1}}{\left(H_2 + \dfrac{\epsilon_t}{2}\right)N_{\mathrm{eff}}}\cdot k_{\mathrm{cl}}} \\ k_{\mathrm{cl}} &= \frac{R_{1,\mathrm{s}}^2 - R_{1,\mathrm{h}}^2}{\left(R_2 - R_{1,\mathrm{s}}\right)\left(1 + \dfrac{\rho_2}{\rho_1}\right)}. \end{aligned} \tag{15}$$

The irreversibility associated to wake mixing at impeller outlet is computed as (Johnston and Dean, 1966)

$$\Delta h_{\mathrm{t,mx}} = \frac{1}{1 + \tan^2(\alpha_2)}\left(\frac{1 - \epsilon_w - H^*}{1 - \epsilon_w}\right)^2\frac{V_2^2}{2}, \tag{16}$$

where the sudden expansion coefficient H^* is fixed to one. To reproduce the efficiency decay observed in the proximity of the choking point, the wake area fraction ϵ_{w} is increased following a geometric progression between the selected minimum and maximum values, i.e., 0.3 and 0.65, once the mass flow rate reaches 80% of the choking point value at the prescribed rotational speed. The flow in the vaneless diffuser is modelled by integrating the system of two-dimensional differential equations derived by Stanitz (1952).

$$\begin{aligned} &V_{\mathrm{m}}\frac{dV_{\mathrm{m}}}{dR} - \frac{V_\theta^2}{R} + C_{\mathrm{f}}\frac{V^2\cos\alpha}{H\sin\chi} + \frac{1}{\rho}\frac{dP}{dR} = 0 \\ &V_{\mathrm{m}}\frac{dV_\theta}{dR} + \frac{V_{\mathrm{m}}V_\theta}{R} + C_{\mathrm{f}}\frac{V^2\cos\alpha}{H\sin\chi} = 0 \\ &\frac{1}{\rho}\frac{d\rho}{dR} + \frac{1}{V_{\mathrm{m}}}\frac{dV_{\mathrm{m}}}{dR} + \frac{1}{H}\frac{dH}{dR} + \frac{1}{R} = 0\frac{dH}{dR} \\ &V_{\mathrm{m}}\frac{dV_{\mathrm{m}}}{dR} + V_{\mathrm{m}}\frac{dV_{\mathrm{m}}}{dR} + V_\theta\frac{dV_\theta}{dR} = 0 \end{aligned} \tag{17}$$

Within this model, the average value of the friction factor is estimated using the empirical correlation proposed by Japikse (1996)

$$C_{\mathrm{f}} = k_{\mathrm{vd}}\left(\frac{1.8\cdot10^5}{Re}\right)^{0.2}. \tag{18}$$

In this work, the value of $k_{\mathrm{vd}} = 0.008$ has been selected as the one providing the best match with experimental data. The losses in the volute and in the exit cone are evaluated in terms of total pressure according to Japikse (1996) and SAE International (2019), respectively, yielding

$$\begin{aligned} \Delta P_{\mathrm{t,vl}} &= \left(K_m + K_\theta\right)\left(P_{\mathrm{t},3} - P_3\right) \\ K_m &= \frac{F_1}{1 + \lambda^2} \quad \text{where } \lambda = \frac{V_{\theta,3}}{V_{\mathrm{m},3}} \\ K_\theta &= F_2\left(\frac{R_3}{R_{\mathrm{vl}}}\right)^2\frac{\left(\lambda - A_3/A_4\right)^2}{1 + \lambda^2} \quad \text{if } \frac{A_4}{A_3}\cdot\lambda > 1 \end{aligned} \tag{19}$$

and

$$\Delta P_{\mathrm{t,cn}} = \rho_3\frac{V_3^2}{2}\frac{8C_{\mathrm{f}}L_{\mathrm{cn}}}{\rho_3 + \rho_4}. \tag{20}$$

In Eqn. (19) the value of both the empirical coefficients F_1 and F_2 is set to 0.8, whereas in Eqn. (20) the friction coefficient, C_{f}, is computed with the Colebrook-White correlation (Colebrook, 1939). The efficiency penalty due to disk friction is estimated as (Daily and Nece, 1960)

$$\begin{aligned} \Delta h_{\mathrm{t,df}} &= K_f\frac{\rho_1 + \rho_2}{2}\frac{R_2^2U_2^3}{4\dot{m}} \\ \text{if } Re_{\mathrm{df}} &= \frac{\rho_2R_2U_2}{\mu_2} < 3\cdot10^5 \quad K_f = \frac{3.7\left(\epsilon_b/H_2\right)^{0.1}}{Re_{\mathrm{df}}^{0.5}} \\ \text{if } Re_{\mathrm{df}} &= \frac{\rho_2R_2U_2}{\mu_2} \geqslant 3\cdot10^5 \quad K_f = \frac{0.102\left(\epsilon_b/H_2\right)^{0.1}}{Re_{\mathrm{df}}^{0.2}}. \end{aligned} \tag{21}$$

The seal leakage loss is accounted for by means of the empirical model of Aungier (2000):

$$\begin{aligned} \Delta h_{\mathrm{t,lk}} &= \frac{\dot{m}_{\mathrm{lk}}U_{\mathrm{lk}}U_2}{2\dot{m}} \\ U_{\mathrm{lk}} &= 0.816\sqrt{\frac{2\Delta P_{\mathrm{lk}}}{\rho_2}} \\ \dot{m}_{\mathrm{lk}} &= \rho_2U_{\mathrm{lk}}N_{\mathrm{eff}}\epsilon_{\mathrm{t}}L_{\mathrm{hd}} \\ \Delta P_{\mathrm{lk}} &= \frac{\dot{m}\left(R_2V_{\theta,2} - R_{1,\mathrm{s}}V_{\theta,1,s}\right)}{N_{\mathrm{eff}}L_{\mathrm{hd}}\dfrac{R_{1,\mathrm{s}} + R_2}{2}\dfrac{H_1 + H_2}{2}}. \end{aligned} \tag{22}$$

The recirculation loss is expressed as (Oh et al., 1997)

$$\Delta h_{\mathrm{t,rc}} = 8\cdot10^{-5}\sinh\left(3.5\cdot\alpha_2^3\right)\left(D_{\mathrm{f}}U_2\right)^2, \tag{23}$$

where the diffusion factor is computed according to Eqn. (14).

3.3. Off-Design Performance

In the following, the procedure adopted to evaluate the compressor characteristic curve along the design speedline is described. The same calculations are iterated at different rotational speeds to construct the compressor operating map.

The choking point is estimated by progressively increasing the mass flow rate from the design point value, and evaluating the meridional Mach number at the outlet of the exducer, together with the relative Mach number at the throat section of the main blade passage. The latter is computed by solving the one-dimensional isentropic flow equations within the control volume defined by the impeller inlet and throat section, at five different span-wise locations:

$$\begin{aligned} &\rho_1W_1\cos\beta_1\frac{2\pi R_1}{N_{\mathrm{bl}}} = \rho_{\mathrm{a}}W_{\mathrm{a}}\left(\frac{2\pi R_1}{N_{\mathrm{bl}}}\cos\beta_{1,\mathrm{bl}} - t_{\mathrm{le}}\right) \\ &h_1 + \frac{W_1^2}{2} - \frac{U_1^2}{2} = h_{\mathrm{a}} + \frac{W_{\mathrm{a}}^2}{2} - \frac{U_{\mathrm{a}}^2}{2} \\ &\rho_{\mathrm{a}} = f(h_{\mathrm{a}}, s_1). \end{aligned} \tag{24}$$

The impeller is considered choked when either the outlet meridional Mach number is equal to one, or the throat Mach number is unitary over the entire blade span.

The minimum mass flow rate at constant rotational speed is limited by the inception of unstable operating conditions, i.e., surge or rotating stall. A conservative estimate can be obtained by assuming that surge is initiated when the slope of the speedline becomes null (Freeman and Cumpsty, 1992), i.e., $d\beta/d\dot{m} = 0$. Due to the complexity of the flow phenomena involved in rotating stall, an accurate prediction of its initiation is only possible by resorting to time-accurate, three-dimensional, full annulus CFD simulations (Marconcini et al., 2017). In the reduced-order model, the inception of rotating stall is estimated using the semi-empirical correlation of Kobayashi et al. (1990)

$$\alpha_{2,c} = \alpha_{2,\text{senoo}} + \left(17.02 - 74.2\frac{H_2}{R_2}\right)\left(1 - \frac{H_3}{H_2}\right), \tag{25}$$

where $\alpha_{2,\text{senoo}}$ refers to the critical flow angle at diffuser inlet computed with the model proposed by Senoo and Kinoshita (1977).

Once the choking point has been estimated, the mass flow rate is progressively reduced, and the compressor performance are computed, until either the conditions of surge, i.e., $d\beta/d\dot{m} \leq 0$, rotating stall inception, i.e., $\alpha_2 > \alpha_{2,c}$, or minimum allowable efficiency, e.g., $\eta_{\text{tt}} < 50\%$, are met. The operating range at the prescribed rotational speed is then computed according to the following definition

$$OR = \frac{\dot{m}_{\text{choke}} - \min(\dot{m})}{\dot{m}_{\text{des}}}. \tag{26}$$

A complete overview of the compressor design workflow is shown in Fig. 3.

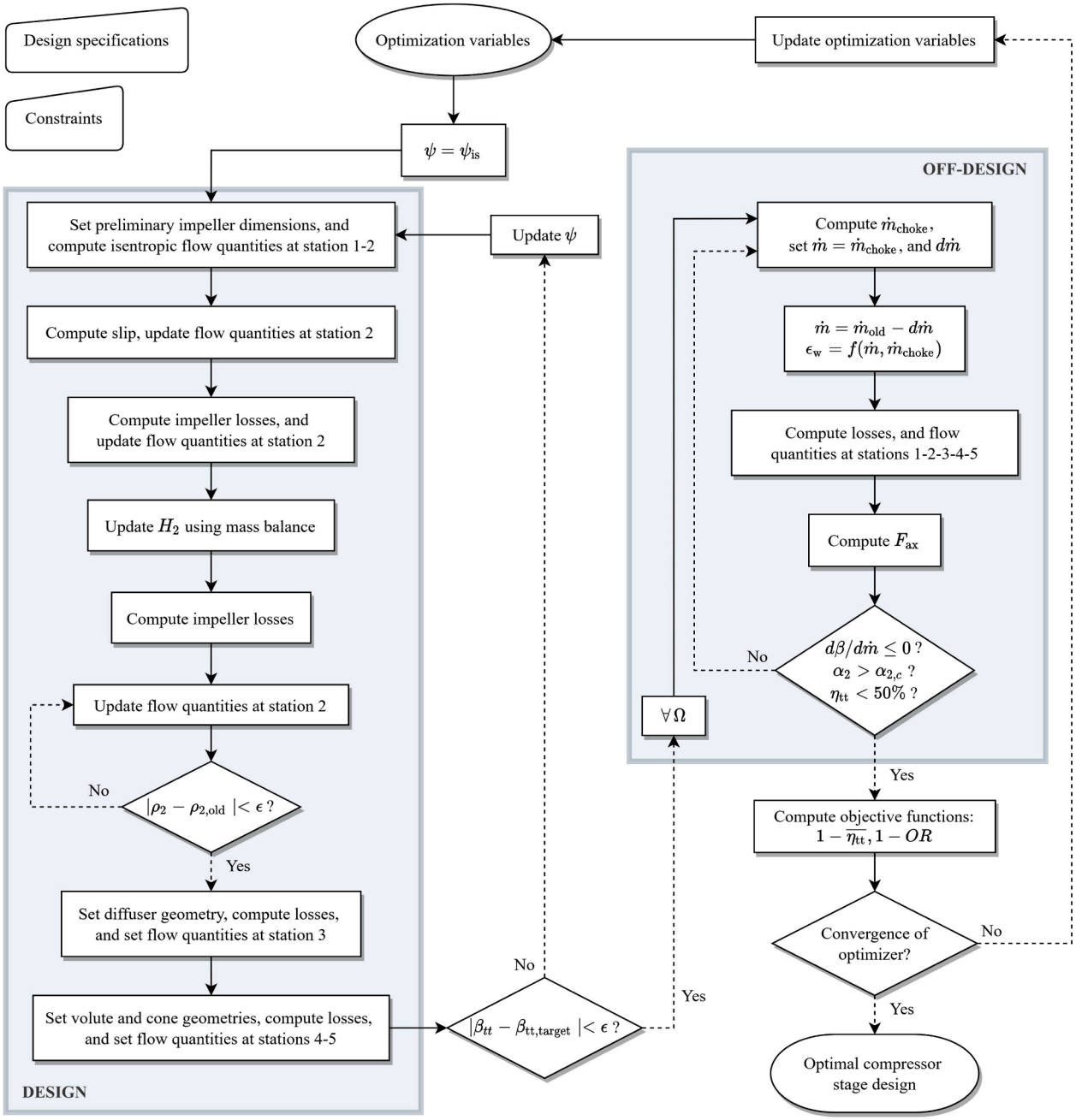

Fig. 3. Flowchart of the reduced-order compressor model: design, off-design, and optimization. The symbol ϵ refers to the tolerance prescribed in the algorithm.

3.4. Validation

In order to assess the accuracy of the tool, the predictions of the compressor model have been compared with experimental data of three well-documented test cases available in the open literature. The first two test cases are the Eckardt impeller O and impeller B (Eckardt, 1975; 1976; 1977; Japikse, 1987), i.e., two large centrifugal compressors featuring a vaneless diffuser, and operating with air. The accuracy of the experimental data is ±1% for the mass flow rate, ±3 rpm for the rotational speed, and ±0.25% for the pressure measured at the nominal location (Japikse, 1987). The third test case is a small-scale compressor designed and tested by Schiffmann and Favrat at EPFL (Schiffmann and Favrat, 2009). The machine features backswept blades, a vaneless diffuser, and operates with refrigerant R134a. The uncertainty of the experimental measurements is ±0.5% for the mass flow rate, and ±0.02 bar for the pressure (Schiffmann and Favrat, 2010). In the analysis presented here, the volute and the exit cone are not modelled, in order to closely reproduce the experimental conditions. The geometrical characteristics and the boundary conditions used to setup the test cases are summarized in Tab. 3.

The results are illustrated in Fig. 4 and Fig. 5. The comparison has been performed over the entire range of rotational speeds for each test case. However, only the efficiency predictions for the EPFL compressor are reported in Fig. 5 for brevity. The outcome of the validation study is that more than 95% of the experimental data fall within the ±5% uncertainty bands of the calculated values, excluding the β_{tt} measurements of the EPFL compressor in the close proximity of the choking point at 210 krpm. Moreover, the semi-empirical correlation proposed by Kobayashi et al. (1990) correctly captures the trend of rotating stall inception, but may lead to underestimation of the operating range for small-scale compressors at large rotational speed. The predictive capabilities of the model may be improved only by resorting to additional experiments or high-fidelity, time-accurate numerical simulations. However, this is beyond the scope of the present work.

4. Design Maps

The validated compressor model is used to generate design maps, namely two-dimensional contours of different performance metrics, computed as a function of Φ_{t1} and β_{tt}, while fixing the values of the remaining independent variables of Eqn. (7). The prescribed ranges of Φ_{t1} and β_{tt} are discretized with 20 sampling points, i.e., each design map presented in the following is constituted by 400 unique compressor designs.

Table 3
Data of the centrifugal compressors used to validate the reduced-order model.

Variable	Eckardt O	Eckardt B	EPFL
Fluid	Air	Air	R134a
T_{t1} [K]	288.15	288.15	283.15
P_{t1} [bar]	1.01	1.01	1.65
Ω [krpm]	10-18	10-16	150-210
$R_{1,s}$ [mm]	140	140	5.6
$R_{1,h}$ [mm]	45	96	1
R_2 [mm]	200	200	10
R_3 [mm]	338	338	16.5
H_2 [mm]	26.7	26.7	1.2
H_3 [mm]	13.6	13.6	1
L_{ax} [mm]	130	84.2	7.7
N_{bl}	20	20	9
N_{split}	0	0	9
$\beta_{1,bl,s}$ [deg]	-63	-60	-60
$\beta_{1,bl,h}$ [deg]	-33	-45	-20.5
$\beta_{2,bl}$ [deg]	0	-40	-45
Ra [mm]	0.01	0.01	0.01
t_{le} [mm]	2.5	2.5	0.2
t_{te} [mm]	1.25	1.25	0.2
ϵ_t [mm]	0.372	0.372	0.05
ϵ_b [mm]	0.372	0.372	0.2
F_0	4.5	4.0	4.0

4.1. Influence of the Working Fluid

The influence of the working fluid on the stage layout and performance is investigated by comparing design maps computed for compressors characterized by the same size parameter $SP = 0.01$ and isentropic work coefficient $\psi_{is} = 0.8$, but operating with different fluids. The working fluids and the corresponding total inlet conditions considered in the present study are listed in Tab. 1. To separately investigate the effect of the fluid molecule and of the compressor size, the values of total inlet pressure and temperature are chosen to guarantee dynamic similarity, i.e., the average Reynolds number based on the hydraulic diameter is kept nearly constant in all test cases. Moreover, the total inlet conditions are selected so that all the fluids are in the dilute gas state, i.e., $\overline{\gamma_{Pv}} \approx \gamma$. Consequently, the influence of flow non-ideality, which is outside the scope of this investigation, can be neglected. However, due to the adoption of the generalized isentropic exponent in the scaling law and in the loss models, the methodology described in this work is applicable also to compressors operating with non-ideal flows, i.e., $\overline{\gamma_{Pv}} \neq \gamma$.

The contours of stage total-to-total efficiency, tip speed Mach number, and relative Mach number at inducer shroud are illustrated in Fig. 6 for air and refrigerant R1233zd(E). The following considerations can be drawn by comparing the two design maps. The compressor stage operating with air features larger values of efficiency over the entire design space, and the performance gap increases when departing from the region of optimal efficiency. Moreover, the fluid molecular complexity affects the shape and the position of the locus of optimal efficiency, as illustrated by the solid black lines. The stage operating with R1233zd(E) features a moderate increment of $M_{W_{1,s}}$ and M_{U_2} over the design space, as highlighted by the dashed red and white lines, respectively. The increase of $M_{W_{1,s}}$ is caused by the lower speed of sound associated to the more complex fluid molecules, whereas the rise of M_{U_2} is due to the smaller value of $\overline{\gamma_{Pv}}$ calculated for R1233zd(E) over the compression process, as discussed in Section 1.

The contours of compressor operating range, and axial thrust acting on bearings are depicted in Fig. 7, for the same couple of working fluids. The main outcomes can be summarized as follows. On the one hand, the stage operating with air is characterized by a wider operating range over the design space. This is mainly due to the smaller value of $M_{W_{1,s}}$ associated to the simpler fluid molecule, which leads to a larger choke margin at design point. On the other hand, the stage operating with air features larger values of axial thrust, as compared to the ones obtained with R1233zd(E). The reason is twofold. First, the two compressor stages are characterized by comparable dimensions, but different total inlet pressure, to achieve dynamic similarity. In turn, the higher inlet pressure imposed to the stage operating with air leads to a larger axial thrust acting on the compressor eye. Furthermore, the air compressor features a higher inlet meridional velocity, thus a larger mass flow rate, and a larger impulse force acting on the inlet.

The previous considerations can be generalized, by analyzing the trends of the stage performance metrics computed for all the working fluids listed in Tab. 1. As illustrated in Fig. 8, an increase of fluid molecular complexity, that is associated to a decrease of $\overline{\gamma_{Pv}}$, leads to a decrease of the optimal value of swallowing capacity. This effect can be attributed to the growing impact of shock losses on impeller performance at increasing values of $M_{W_{1,s}}$, observed in correspondence of small values of γ_{Pv} and large values of Φ_{t1}. Moreover, the optimal stage efficiency is directly proportional to $\overline{\gamma_{Pv}}$ and inversely proportional to the target pressure ratio, see Fig. 8. The rotational speed at design point shows an opposite trend, as displayed in Fig. 9. To summarize, given the compressor scale, measured by SP, and the isentropic work coefficient ψ_{is}, the stages operating with working fluids made of simple molecules,

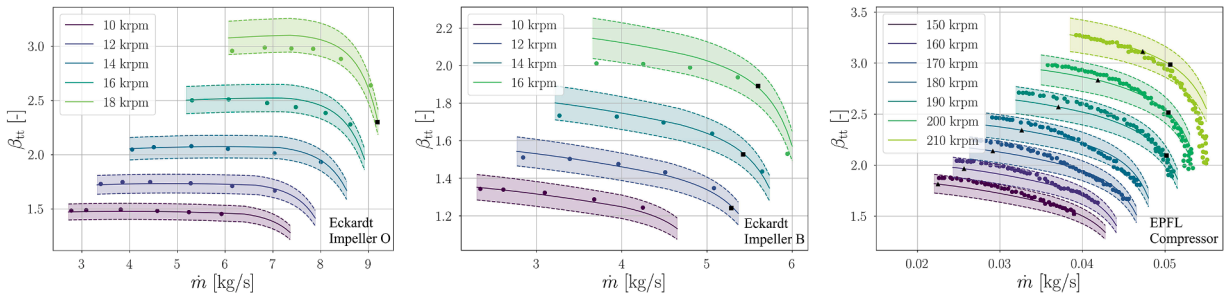

Fig. 4. Total-to-total pressure ratio vs. mass flow rate. Solid lines represent compressor model predictions; dashed lines bound colored ±5% uncertainty bands; dots correspond to experimental data of Eckardt impellers O and B (Eckardt, 1977; Japikse, 1987), and EPFL compressor (Schiffmann and Favrat, 2010). The estimated choking and rotating stall operating points are marked by ■ and ▲, respectively.

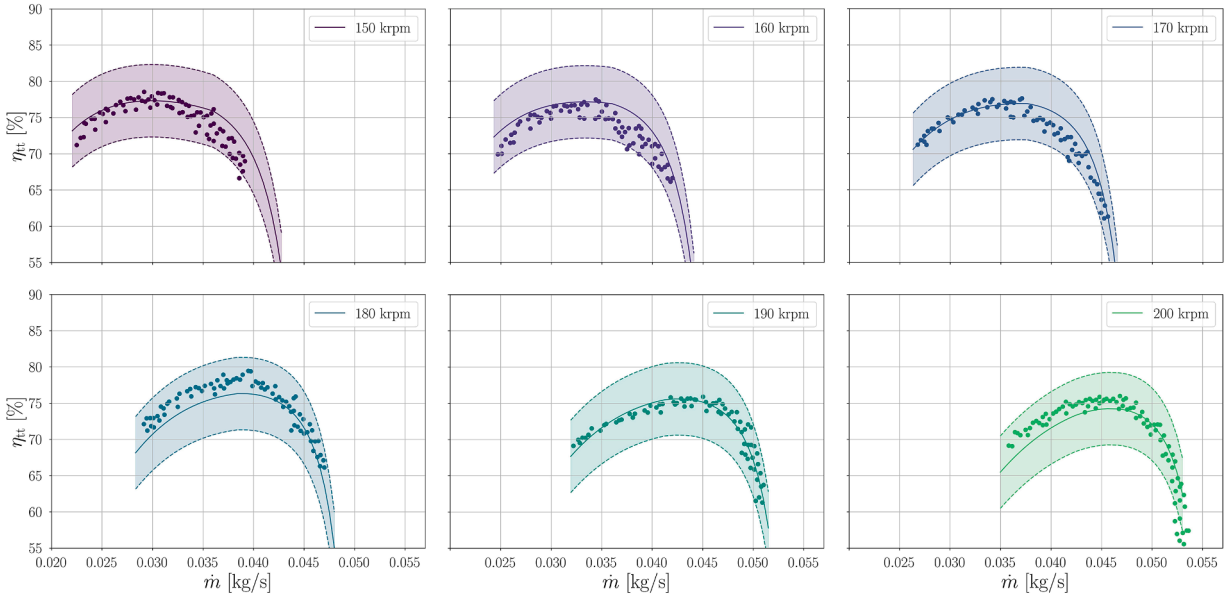

Fig. 5. Total-to-total efficiency vs. mass flow rate for the EPFL compressor. Solid lines represent compressor model predictions; dashed lines bound colored ±5% uncertainty bands; dots correspond to experimental data (Schiffmann and Favrat, 2010).

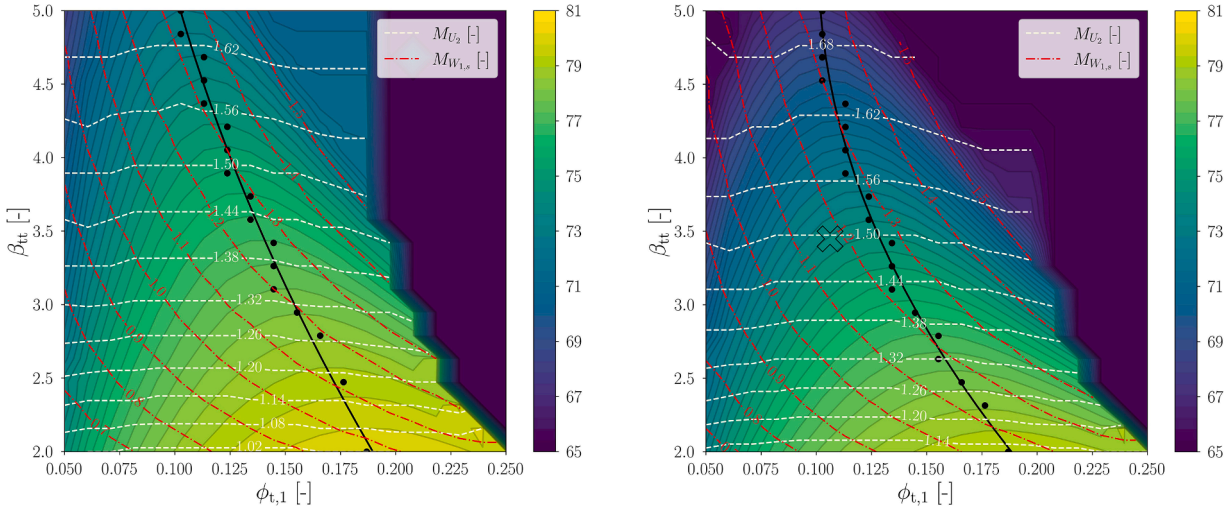

Fig. 6. Design maps of η_{tt}, M_{U_2}, and $M_{W_{1,s}}$, computed for air and refrigerant R1233zd(E) at $\psi_{is} = 0.8$, $SP = 0.01$, $k = 0.9$, and at P_{t1}, T_{t1} specified in Tab. 1. The dots correspond to the values of Φ_{t1} that maximize η_{tt} for each β_{tt}; the solid line represents their spline interpolation of order two. The cross indicates the design point resulting from the optimization study described in Section 5.

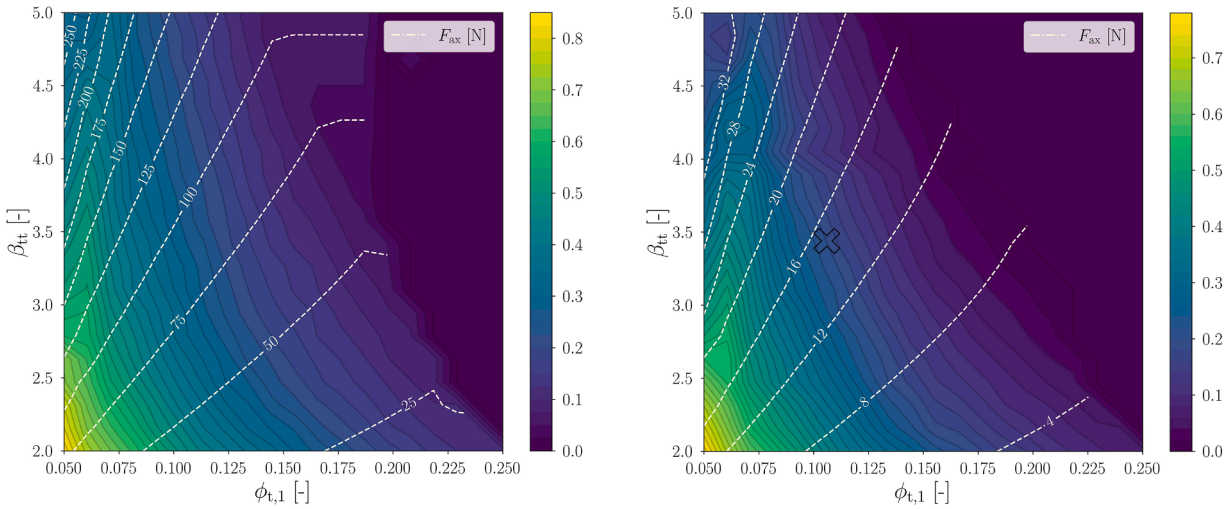

Fig. 7. Design maps of OR, and F_{ax}, computed for air and refrigerant R1233zd(E) at $\psi_{is} = 0.8$, $SP = 0.01$, $k = 0.9$, and at P_{t1}, T_{t1} specified in Tab. 1. The cross indicates the design point resulting from the optimization study described in Section 5.

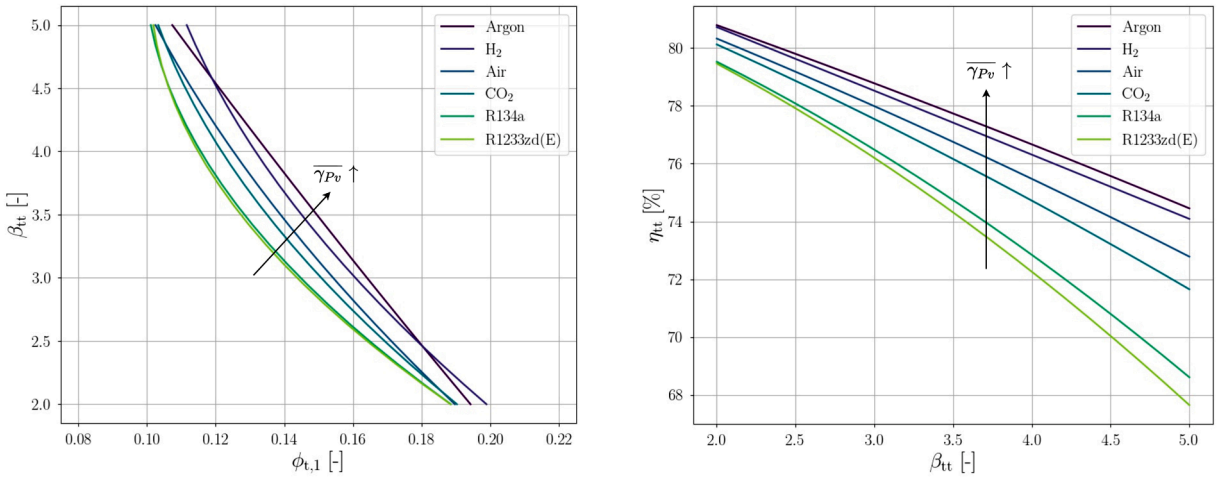

Fig. 8. Locus of optimal efficiency for compressors operating with fluids of increasing molecular complexity. All the computations are performed with $\psi_{is} = 0.8$, $SP = 0.01$, $k = 0.9$, and at P_{t1}, T_{t1} specified in Tab. 1.

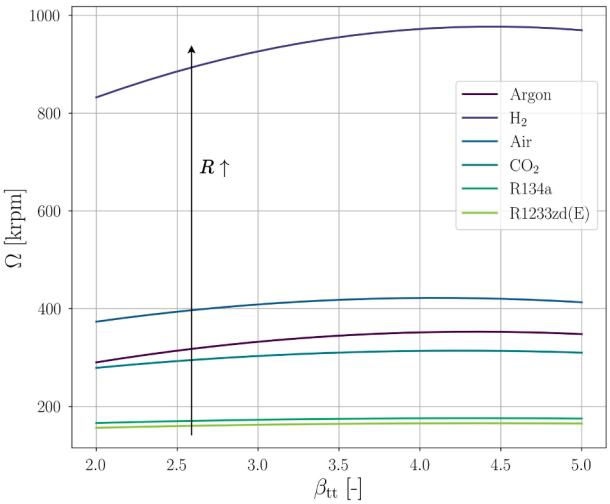

Fig. 9. Rotational speed computed along the locus of optimal efficiency for the test cases listed in Tab. 1

characterized by large values of $\overline{\gamma_{Pv}}$ and R, are more efficient, but their rotational speed is higher. As a consequence, Ω may exceed the maximum allowable limit for mechanical resistance, and the stage must be re-designed at higher work coefficient, at the expenses of fluid dynamic efficiency. Fluid molecules like Argon, featuring high values of isentropic exponent and relatively high molecular weight, are attractive, as they enable the design of mini compressors characterized by both high efficiency and moderate rotational speed.

4.2. *Influence of Size*

The influence of scale on compressor design is studied by comparing design maps computed for stages operating with Air and R1233zd(E), but characterized by different values of size parameter $SP = 0.1 - 0.05 - 0.01$. The total inlet conditions are kept unaltered, but the dynamic similarity condition is not valid anymore, due to the different compressor dimensions. Moreover, the magnitude of relative clearances and relative surface roughness decreases with increasing size parameter, due to the relaxation of manufacturing constraints.

The stages featuring larger size parameter are characterized by higher efficiency values over the entire design space, as shown in Fig. 10. However, the size parameter has only a minor influence on the

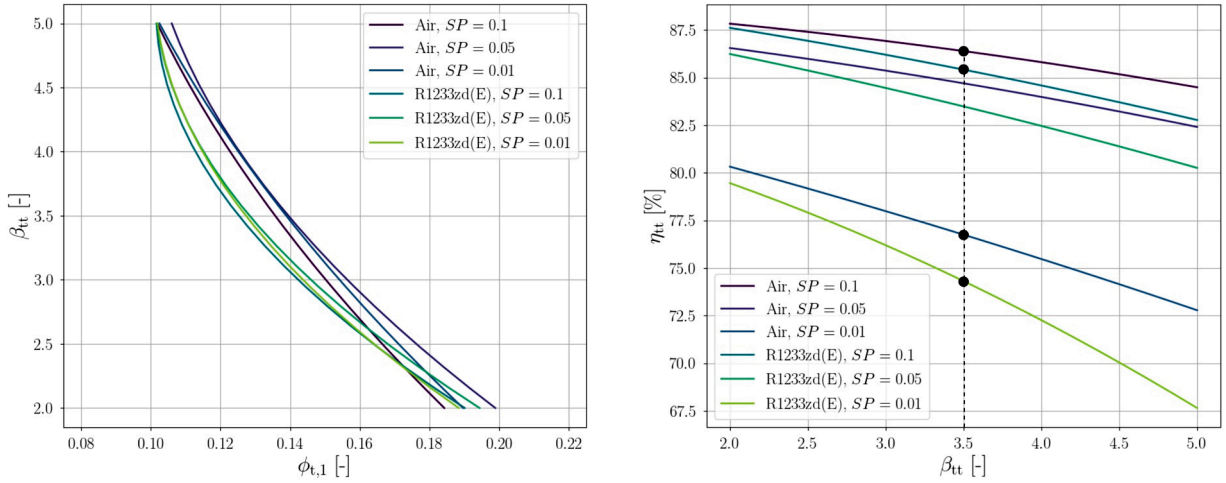

Fig. 10. Locus of optimal efficiency for compressors characterized by different size parameter. All the computations are performed at $\psi_{is} = 0.8$, $k = 0.9$, and at P_{t1}, T_{t1} specified in Tab. 1. The black dots correspond to the stage designs chosen for the loss breakdown analysis.

locus of optimal efficiency in the $\Phi_{t1} - \beta_{tt}$ plane. To gain further insights about the sources of efficiency penalty in small-scale compressors, a detailed loss breakdown analysis has been performed for stages with varying size parameter, and designed at moderate pressure ratio in the neighborhood of the optimal efficiency region, i.e., $SP = 0.1 - 0.01$, $\beta_{tt} = 3.5$, $\Phi_{t1} = 0.13$, see Fig. 11. The loss sources that are mostly affected by the change of *SP* are the ones associated to tip clearance, seal leakage, recirculation, and viscous friction in the impeller and the diffuser. The increase of recirculation loss at low values of size parameter is induced by the rise of the optimal α_2 computed by the reduced-order model, and thus cannot be significantly mitigated. On the contrary, the increase of clearance and leakage losses can be alleviated by reducing the relative tip gap. In the same fashion, the efficiency penalties due to viscous friction can be mitigated by reducing the relative surface roughness. Quantifying the impact of the different manufacturing constraints on the stage efficiency is of paramount importance to focus efforts and resources in the areas that can enable the largest performance gain. The calculations performed with the reduced-order model show that an increase of relative tip gap of one order of magnitude leads to an efficiency penalty of $\approx 6\%$ for the stage operating with refrigerant R1233zd(E). In the same fashion, an increase of relative surface roughness of one order of magnitude produces a performance decay of the order of 3.8%. Similar trends are calculated for the air compressor.

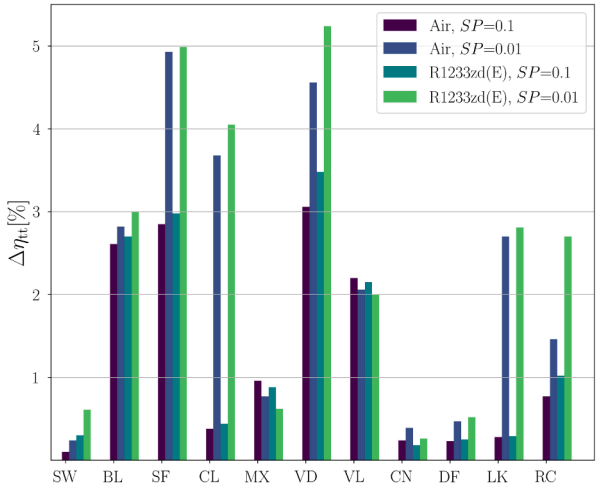

Fig. 11. Loss breakdown for compressor stages operating with air and refrigerant R1233zd(E), featuring $\Phi_{t1} = 0.13$, $\psi_{is} = 0.8$, $\beta_{tt} = 3.5$, $SP = 0.1 - 0.01$. The abbreviations displayed on the abscissa refer to the subscripts used to identify the loss components.

To summarize, the value of swallowing capacity maximizing the stage efficiency is not remarkably influenced by the size parameter and lies between $\Phi_{t1} = 0.1 - 0.15$ for stages featuring moderate to high pressure ratio. However, the stage operating range is maximum at low values of swallowing capacity, i.e., $\Phi_{t1} = 0.05 - 0.07$. A similar argument can be used to prove that there is a trade-off between stage efficiency and operating range with respect to most of the design variables listed in Eqn. 7. Therefore, the optimal design of this kind of machines can be achieved only by resorting to a multi-objective optimization strategy.

5. Multi-Objective Design Optimization

In order to verify the validity of the design guidelines derived from the maps presented in Section 4, a design exercise was carried out, namely the multi-objective optimization of the first compressor stage that will be installed in the IRIS test rig. The selected case study is particularly relevant, as it features small dimensions, a working fluid of moderate molecular complexity, and stringent requirements in terms of both efficiency and operating range. The simplified process flow diagram of the test rig is shown in Fig. 1. It consists of a two pressure level refrigeration cycle resembling the configuration of an ECS for large helicopters, i.e., nineteen passengers and two pilots.

In mathematical form, the multi-objective design optimization of a single stage centrifugal compressor can be formulated as follows:

$$\begin{aligned} &\min_{\boldsymbol{x}\in\mathbb{R}^n} \boldsymbol{F}(\boldsymbol{x}) = \left[f_1(\boldsymbol{x}), \ldots, f_{n_{obj}}(\boldsymbol{x})\right], \quad \text{s.t.} \\ &h_k(\boldsymbol{x}) = 0 \quad k = 1, \ldots, n_{eq} \\ &g_i(\boldsymbol{x}) \leq 0 \quad i = 1, \ldots, n_{ineq} \\ &x_{l,j} \leq x_j \leq x_{u,j} \quad j = 1, \ldots, n \end{aligned} \tag{27}$$

where $\boldsymbol{x}$ is the vector of independent variables, $\boldsymbol{F}(\boldsymbol{x}) = [1 - \eta_{tt},\ 1 - OR]$ is the vector of the objective functions, and $h_k(\boldsymbol{x})$, $g_i(\boldsymbol{x})$ are the vectors of the equality and inequality constraints, respectively. The parameters, the optimization variables, and the inequality constraints considered in the present work are listed in Tab. 4. Overall, the optimization problem comprises eight design variables, two objectives, and seven inequality constraints.

5.1. Optimization Results

The Pareto front is computed by means of the NSGA-II algorithm described in (Deb et al., 2002) and implemented in (Blank and Deb,

Table 4
Setup of the multi-objective compressor design optimization.

Variable	Type	Value
β_{tt}	Parameter	3.45
$\dot{m}$ [kg/s]	Parameter	0.114
fluid	Parameter	R1233zd(E)
P_{t1} [kPa]	Parameter	47.789
T_{t1} [K]	Parameter	278.13
Φ_{t1}	Design variable	0.05-0.2
ψ_{is}	Design variable	0.6-1.0
α_2 [deg]	Design variable	60-75
k	Design variable	0.65-0.95
N_{bl}	Design variable	12-20
R_3/R_2	Design variable	1.3-2.0
$\frac{H_3 - H_2}{H_2(R_2/R_{pinch} - 1)}$	Design variable	0-1
$\frac{R_{pinch} - R_2}{R_3 - R_2}$	Design variable	0-1
$\min(R_{1,h})$ [mm]	Ineq. constraint	3.25
$\max(R_4)$ [mm]	Ineq. constraint	50
$\min(a)$ [mm]	Ineq. constraint	1.0
$\min(H_2)$ [mm]	Ineq. constraint	1.35
$\max(\Omega)$ [krpm]	Ineq. constraint	150
$\max(F_{ax})$ [N]	Ineq. constraint	50
$\max(M_3)$	Ineq. constraint	0.65

2020). All the optimization variables are floating point, except for the number of blades, which is treated as an integer. The initial population comprises ten individuals for each design variable and is sampled according to the latin hypercube methodology along the floating point directions, and randomly along the integer axis. The population is evolved for eighty generations, applying simulated binary crossover and polynomial mutation, leading to 6400 function evaluations. As displayed in Fig. 12, the resulting Pareto front shows larger variability over the axis associated to compressor operating range than over the one related to stage isentropic efficiency. In turn, the optimal conceptual design has been chosen among the non-dominated solutions by prioritizing the compressor operating range as objective.

The main features of the optimal design are reported in Tab. 5, while the meridional view of the resulting impeller and diffuser is displayed in Fig. 12. The optimal compressor design is characterized by $\psi_{is} \approx 0.8$, $SP \approx 0.01$, and $k \approx 0.9$, thus the corresponding design point can be displayed on the maps shown in Fig. 6-7. Three main considerations can be outlined.

As expected, the swallowing capacity of the optimal design lies in between the locus of optimal efficiency and the region of maximum operating range. The higher is the prescribed pressure ratio, and the molecular complexity of the selected working fluid, the smaller is the distance between the locii of maximum efficiency and operating range. This information is essential to address the trade-off between design point efficiency and operability, when approaching the design of a new prototype.

Table 5
Main characteristics of the compressor design selected along the Pareto front generated by the reduced-order model coupled to a gradient-free optimizer.

Variable	Value	Variable	Value
N_s	1.208	D_s	1.870
$M_{W_{1,s}}$	1.12	M_{U_2}	1.5
Φ_{t1}	0.106	ψ_{is}	0.793
SP	0.019	k	0.95
Ω [krpm]	68-94	$\beta_{1,bl,s}$ [deg]	60
$R_{1,s}$ [mm]	15.2	$\beta_{1,bl,h}$ [deg]	16.5
$R_{1,h}$ [mm]	3.4	$\beta_{2,bl}$ [deg]	29.6
R_2 [mm]	22.8	Ra [mm]	0.032
R_3 [mm]	35.2	R_4 [mm]	49.3
H_2 [mm]	2.3	$D_{cn,out}$ [mm]	17.8
H_3 [mm]	1.6	t_s [mm]	0.3
L_{ax} [mm]	16.0	t_h [mm]	0.6
N_{bl}	7	ϵ_t [mm]	0.15
N_{split}	7	ϵ_b [mm]	0.15

The tip speed Mach number and the relative Mach number at the inducer shroud can be accurately predicted from the design maps. The tip speed Mach number scales with the prescribed pressure ratio, whereas the relative Mach number is also a function of the swallowing capacity. In the proposed design exercise, in order to comply with the requirement of subsonic flow in the inducer, one has to select a lower swallowing capacity, thus further compromising on the design point efficiency.

The optimal design is not located on the Cordier line, i.e., the locus of optimal efficiency in the $N_s - D_s$ chart (Balje, 1981), where

$$N_s = \Omega \frac{\dot{V}_1^{1/2}}{\Delta h_{ts}^{3/4}}, \tag{28}$$

$$D_s = D_1 \frac{\Delta h_{ts}^{1/4}}{\dot{V}_1^{1/2}}. \tag{29}$$

Therefore, such design cannot be obtained by applying existing design rules.

5.2. Performance Investigation based on CFD

The three-dimensional geometry of the impeller and the diffuser are constructed from the conceptual design data of the optimal compressor design, using a commercial software (ANSYS Inc., 2019a). The shape of the main and the splitter blades are controlled by specifying the hub, mid, and shroud profiles, and by stacking them along the radial direction

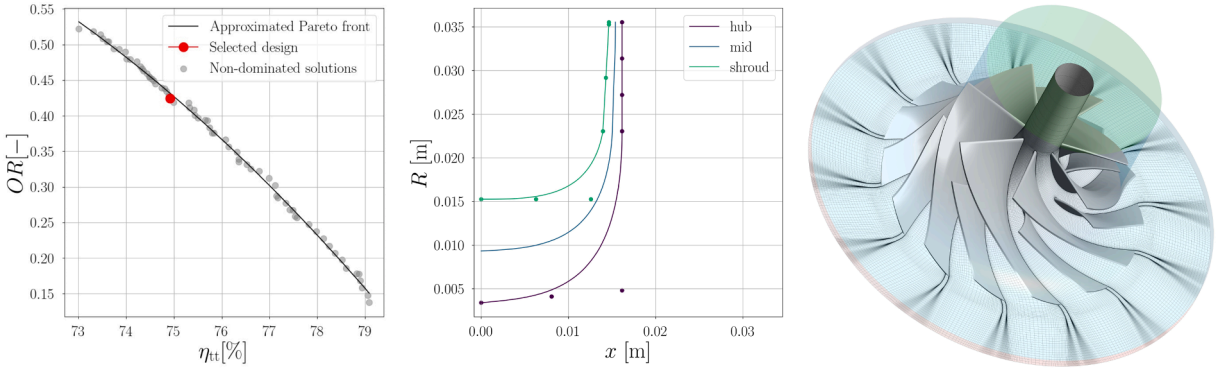

Fig. 12. Optimal design of the first compressor stage for the IRIS test rig. From left to right: Pareto front obtained with the multi-objective optimization framework, meridional flow path of the selected design, 3D impeller geometry and computational grid. The hub and shroud curves are defined as third order Bezier curves, whose control points are displayed in the central image.

at leading edge. To cope with transonic flow in the inducer, the blades are designed to be aft-loaded at shroud, aiming to improve the choke margin and reduce the shock losses (Casey and Robinson, 2021). The wrap angle at each span-wise location is set to obtain 16.5° of rake angle, to enhance the structural integrity of the impeller. The blades feature constant thickness distribution in the meridional direction and linear tapering in the span-wise direction. The vaneless diffuser is characterized by a linear pinch extending through its entire length. The presence of the volute is neglected in this analysis to reduce the computational cost.

Steady-state, single passage RANS computations (ANSYS Inc., 2019b) with a mixing-plane interface are used to assess the compressor fluid dynamic performance over the entire operating range. The boundary conditions are imposed in terms of flow direction, total pressure, and total temperature at the inlet, whereas the mass flow rate is assigned at the outlet. The $\kappa - \omega$ SST turbulence model is employed together with adequate cell clustering near walls to guarantee $y^+ \leq 1$. Turbulence boundary conditions are set in terms of inlet turbulence intensity ($\kappa = 5\%$) and eddy viscosity ratio ($\mu/\mu_t = 10$), while the turbulent Prandtl number is set to $Pr_t = 1$, in accordance with what is documented in (Otero et al., 2018). The advective and turbulent fluxes are discretized with total variation diminishing schemes (Barth and Jespersen, 1989), while a central difference scheme is adopted for discretizing the viscous fluxes. A look-up table method is employed to speed-up the evaluation of the thermo-physical fluid properties. The property values are calculated using the multi-parameter equation of state model available in (Lemmon et al., 2018). The vapor properties are extended up to the spinodal line to improve solver robustness in the initial phase of the calculation, without affecting the accuracy of the converged solution. After performing a sensitivity analysis, see Fig. 13, a grid size of approximately two million cells and a thermodynamic mesh of one million elements are set as optimal trade-off between accuracy and computational cost.

A total of 27 RANS computations have been performed to compute the compressor operating map in a range of rotational speeds extending from 80% to 110% of the design point value, corresponding to 85.7 krpm, as shown in Fig. 14. The CFD calculations determined a design point pressure ratio of 3.38 and an isentropic efficiency equal to 85.93%, neglecting the effect of parasitic losses, and of the efficiency decay in the volute and the exit cone. The maximum deviation between the predictions of the reduced-order model and CFD is 6.18% and 6.86% in terms of β_{tt} and η_{tt}, respectively, whereas the average deviation measured for both performance metrics is below 5%. These results provide further evidence of the accuracy of the in-house tool, and additional confidence in the trends described in Section 4.

Further insights about the compressor flow field at design point can

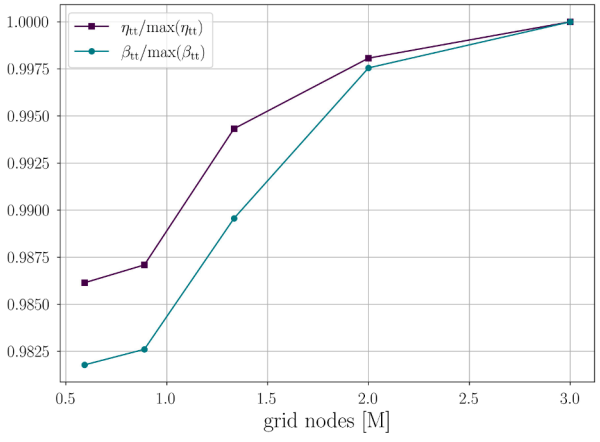

Fig. 13. Sensitivity of total-to-total pressure ratio and internal isentropic efficiency on the number of grid nodes.

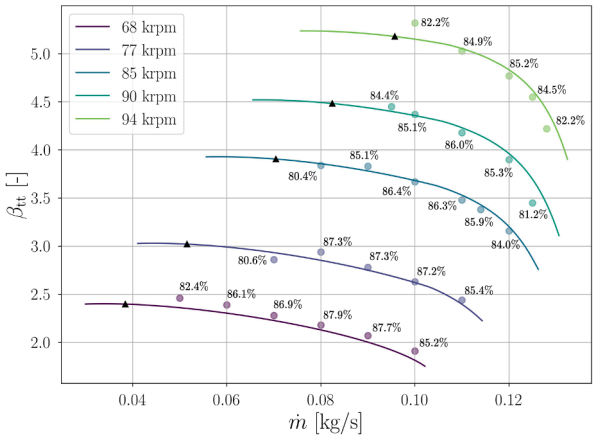

Fig. 14. Compressor operating map. The solid lines represent the predictions of the reduced-order model; the results computed by CFD are displayed by the dots, in terms of both mass-flow averaged β_{tt} and internal η_{tt}.

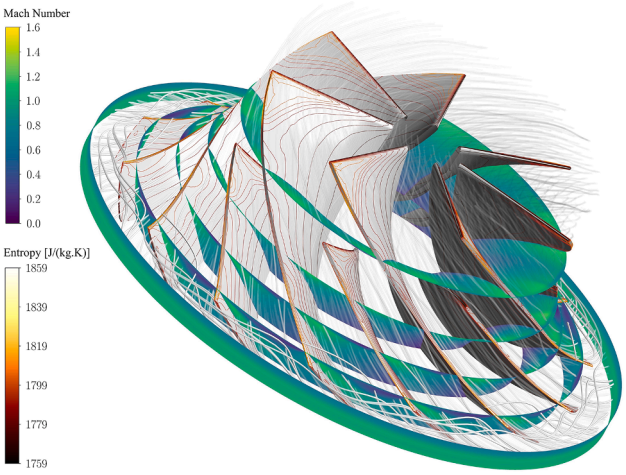

Fig. 15. Flow field computed by means of CFD at design point. The Mach number distribution is shown in the form of contour plots over different secondary planes. The iso-entropy lines are displayed over the blade surfaces. 3D streamlines are colored from transparent to white, according to the local value of entropy, to highlight the tip leakage vortex.

be gained by inspecting Fig. 15. The largest entropy generation is predicted in the shroud region of the inducer, due to the occurrence of transonic Mach number, and in the rear part of the blades, as a result of viscous mixing of the tip leakage vortex with the main flow. As highlighted by the streamlines, the use of aft-loaded blades at shroud is effective in delaying the formation of the tip leakage vortex, thus reducing the efficiency penalty associated to large tip clearance, as reported in (Javed et al., 2016). More advanced three-dimensional design strategies, supported by a CFD-based optimization framework, see (Elfert et al., 2017), can be used to further refine the candidate design, enabling even higher efficiency and wider operating range.

6. Conclusions

The effect of size and working fluid on the efficiency, operating range, and axial thrust on bearings has been investigated for single stage centrifugal compressors by means of a reduced-order model, validated with experimental data. Moreover, the reduced-order model has been used to perform a design exercise, i.e., the multi-objective optimization of the first compressor stage of the heat pump test rig currently under construction at Delft University of Technology. The key characteristics

of the optimal compressor design have been compared to those derived from the design maps, to corroborate their validity. The optimal design has been extensively characterized by means of 3D steady RANS simulations. The outcomes of this study can be summarized as follows.

1. Compressor stages operating with fluids made of heavy and complex molecules exhibit lower efficiency, if compared to compressors for fluids made of simpler molecules. The locus of optimal efficiency shifts towards lower values of swallowing capacity for decreasing values of $\overline{\gamma_{Pv}}$. However, compressors operating with simple-molecule fluids optimally operate with higher rotational speed. If Ω exceeds the maximum allowable threshold, the stage should be re-designed at higher work coefficient, therefore penalizing fluid dynamic performance.
2. Fluid molecular complexity has a minor influence on the stage operating range, but it remarkably affects the axial thrust acting on the bearings. Compressor stages operating with complex-molecule fluids produce lower axial thrust, if compared to their simple-molecule counterparts, thus making them particularly suitable for the use of oil-free gas bearings.
3. Compressors featuring a lower size parameter are characterized by lower efficiency, as a result of manufacturing constraints, leading to higher relative tip clearance and higher relative surface roughness. The efficiency penalty is more sensitive to variations of clearance gap than to surface finishing. However, the size parameter has a negligible influence on the shape and the position of the locus of optimal efficiency.
4. The optimal design of the first compressor stage for the IRIS test rig complies with the guidelines that can be derived from the $\Phi_{t1} - \beta_{tt}$ maps, in terms of design point efficiency, operating range, tip speed Mach number and relative Mach number at the inducer shroud. Moreover, the optimal design can not be readily obtained by applying existing design rules, as it is not located on the Cordier line in the $N_s - D_s$ chart.
5. Steady-state RANS simulations of the flow past the optimal compressor layout predict a design point pressure ratio of $\beta_{tt} = 3.38$, an internal isentropic efficiency equal to $\eta_{is} = 85.93\%$, and an operating range of 0.49 at 85.7 krpm. These findings provide further evidence that efficient mini-compressors operating with organic fluids, and featuring pressure ratios up to five at off-design conditions, are feasible from the fluid dynamic standpoint.

Metadata

The geometry of the compressor stage obtained as a result of the multi-objective design optimization, and the full set of design maps, (omitted here for brevity) can be downloaded at the website link[1].

CRediT authorship contribution statement

Andrea Giuffre: Conceptualization, Methodology, Software, Validation, Data curation, Writing – original draft. **Piero Colonna:** Funding acquisition, Project administration, Writing – review & editing. **Matteo Pini:** Conceptualization, Supervision, Writing – review & editing.

Declaration of Competing Interest

The authors declare that they have no known competing financial interests or personal relationships that could have appeared to influence the work reported in this paper.

[1] https://github.com/Propulsion-Power-TU-Delft/Metadata/tree/main/IRISCompressor

Acknowledgements

The authors gratefully acknowledge Prof. Jürg Schiffmann for providing the geometrical data of the compressor tested at EPFL and Prof. Michael Casey for his seminal work and his valuable suggestions about centrifugal compressor design. This research was supported by the Dutch Technology Foundation TTW, Applied Science Division of NWO, the Technology Program of the Ministry of Economic Affairs, and by Aeronamic BV (Grant No. 17091).

Supplementary material

Supplementary material associated with this article can be found, in the online version, at 10.1016/j.ijrefrig.2022.06.023

References

ANSYS Inc., 2019a. ANSYS Academic Research BladeGen, Release 19.3. http://www.ansys.com.
ANSYS Inc., 2019b. ANSYS Academic Research CFX, Release 19.3. http://www.ansys.com.
Aungier, R.H., 2000. Centrifugal Compressors: A Strategy for Aerodynamic Design and Analysis. ASME Press. https://doi.org/10.1115/1.800938.
von Backström, T.W., 2006. A unified correlation for slip factor in centrifugal impellers. Journal of Turbomachinery 128 (1), 1–10. https://doi.org/10.1115/1.2101853.
Balje, O., 1981. Turbomachines: a guide to design, selection and theory. Wiley, New York.
Barth, T., Jespersen, D., 1989. The design and application of upwind schemes on unstructured meshes10.2514/6.1989-366.
Bender, D., 2018. Exergy-based analysis of aircraft environmental control systems and its integration into model-based design.
Blank, J., Deb, K., 2020. Pymoo: Multi-Objective Optimization in Python. IEEE Access 8, 89497–89509. https://doi.org/10.1109/ACCESS.2020.2990567.
Boeing, 2007. AERO, 4th quarterhttps://www.boeing.com/commercial/aeromagazine/articles/qtr_4_07/index.html.
Brasz, J.J., 1988. Investigation into the Effect of Tip Clearance on Centrifugal Compressor Performance. Technical Report.http://asmedigitalcollection.asme.org/GT/proceedings-pdf/GT1988/79184/V001T01A066/4456891/v001t01a066-88-gt-190.pdf
Came, P.M., Robinson, C.J., 1998. Centrifugal compressor design. Proceedings of the Institution of Mechanical Engineers, Part C: Journal of Mechanical Engineering Science 213 (2), 139–155. https://doi.org/10.1243/0954406991522239.
Casey, M., Robinson, C., 2021. Radial Flow Turbocompressors: Design, Analysis, and Applications, 1st. Cambridge University Press. https://doi.org/10.1017/9781108241663.
Casey, M.V., Krähenbühl, D., Christof, Z., 2013. The Design of Ultra-High-Speed Miniature Centrifugal Compressors. European Conference on Turbomachinery Fluid Dynamics and Thermodynamics.
Colebrook, C.F., 1939. Turbulent Flow in Pipes, with Particular Reference to the Transition Region Between the Smooth and Rough Pipe Laws. Journal of the Institution of Civil Engineers 11 (4), 133–156. https://doi.org/10.1680/ijoti.1939.13150.
Coppage, J., Dallenbach, F., Eichenberger, H., Hlavaka, G., Knoernschild, E., Van Lee, N., 1956. Study of Supersonic Radial Compressors for Refrigeration and Pressurization on Systems, WADC 55–257https://apps.dtic.mil/sti/citations/AD0110467.
Daily, J.W., Nece, R.E., 1960. Chamber dimension effects on induced flow and frictional resistance of enclosed rotating disks. Journal of Fluids Engineering, Transactions of the ASME 82 (1), 217–230. https://doi.org/10.1115/1.3662532.
Deb, K., Pratap, A., Agarwal, S., Meyarivan, T., 2002. A fast and elitist multiobjective genetic algorithm: NSGA-II. IEEE Transactions on Evolutionary Computation 6 (2), 182–197. https://doi.org/10.1109/4235.996017.
Denton, J.D., 1993. Loss mechanisms in turbomachines. Journal of Turbomachinery 115 (4), 621–656. https://doi.org/10.1115/1.2929299.
Eckardt, D., 1975. Instantaneous measurements in the jet-wake discharge flow of a centrifugal compressor impeller. Journal of Engineering for Gas Turbines and Power 97 (3), 337–345. https://doi.org/10.1115/1.3445999.
Eckardt, D., 1976. Detailed flow investigations within a high-speed centrifugal compressor impeller. Journal of Fluids Engineering, Transactions of the ASME 98 (3), 390–399. https://doi.org/10.1115/1.3448334.
Eckardt, D., 1977. Doctoral Dissertation. Technical Report.https://ntrs.nasa.gov/api/citations/19780008108/downloads/19780008108.pdf?attachment=true
Elfert, M., Weber, A., Wittrock, D., Peters, A., Voss, C., Nicke, E., 2017. Experimental and numerical verification of an optimization of a fast rotating high-performance radial compressor impeller. Journal of Turbomachinery 139 (10). https://doi.org/10.1115/1.4036357/378792.
Freeman, C., Cumpsty, N.A., 1992. Method for the prediction of supersonic compressor blade performance. Journal of Propulsion and Power 8 (1), 199–208. https://doi.org/10.2514/3.23461.
Galvas, M.R., 1973. Fortran Program for Predicting Off-Design Performance of Centrifugal Compressors. Technical Report.

Giuffre', A., Pini, M., 2021. Design Guidelines for Axial Turbines Operating With Non-Ideal Compressible Flows. Journal of Engineering for Gas Turbines and Power 143 (1). https://doi.org/10.1115/1.4049137.

Heshmat, H., Walton, J.F., Corte, C.D., Valco, M., 2000. Oil-free turbocharger demonstration paves way to gas turbine engine applications. Proceedings of the ASME Turbo Expo. American Society of Mechanical Engineers (ASME). https://doi.org/10.1115/2000-GT-0620.

Jansen, W., 1970. A method for calculating the flow in a centrifugal impeller when entropy gradient are present. Inst. Mech. Eng. Internal Aerodynamics.https://ci.nii.ac.jp/naid/10015075565

Japikse, D., 1987. A critical evaluation of three centrifugal compressors with pedigree data sets: Part 5-studies in component performance. Journal of Turbomachinery 109 (1), 1–9. https://doi.org/10.1115/1.3262064.

Japikse, D., 1996. Centrifugal Compressor Design and Performance. Concepts Eti.https://www.amazon.com/Centrifugal-Compressor-Design-Performance-Japikse/dp/0933283032

Javed, A., Arpagaus, C., Bertsch, S., Schiffmann, J., 2016. Turbocompresseurs de petite taille pour un fonctionnement sur une large plage avec des jeux radiaux importants pour un concept de pompe à chaleur bi-étagée. International Journal of Refrigeration 69, 285–302. https://doi.org/10.1016/j.ijrefrig.2016.06.015.

Jeong, Y., Son, S., Cho, S.K., Baik, S., Lee, J.I., 2020. Evaluation of supercritical CO2 compressor off-design performance prediction methods. Energy 213, 119071. https://doi.org/10.1016/J.ENERGY.2020.119071.

Johnston, J.F., Dean, R.C., 1966. Losses an vaneless diffusers of centrifugal compressors and pumps: Analysis, experiment, and design. Journal of Engineering for Gas Turbines and Power 88 (1), 49–60. https://doi.org/10.1115/1.3678477.

Kobayashi, H., Nishida, H., Takagi, T., Fukushima, Y., 1990. A study on the rotating stall of centrifugal compressors. II - Effect of vaneless diffuser inlet shape on rotating stall. JSMET 56, 2646–2651.https://ui.adsabs.harvard.edu/abs/1990JSMET..56.2646K/abstract

Kouremenos, D.A., Kakatsios, X.K., 1985. The three isentropic exponents of dry steam. Forschung im Ingenieurwesen 51 (4), 117–122. https://doi.org/10.1007/BF02558416.

Lemmon, E. W., Bell, I. H., Huber, M. L., McLinden, M. O., 2018. NIST Standard Reference Database 23: Reference Fluid Thermodynamic and Transport Properties-REFPROP, Version 10.0, National Institute of Standards and Technology. 10.18434/T4/1502528.

Marconcini, M., Bianchini, A., Checcucci, M., Ferrara, G., Arnone, A., Ferrari, L., Biliotti, D., Rubino, D.T., 2017. A three-dimensional time-accurate computational fluid dynamics simulation of the flow field inside a vaneless diffuser during rotating stall conditions. Journal of Turbomachinery 139 (2). https://doi.org/10.1115/1.4034633.

Oh, H.W., Yoon, E.S., Chung, M.K., 1997. An optimum set of loss models for performance prediction of centrifugal compressors. Proceedings of the Institution of Mechanical Engineers, Part A: Journal of Power and Energy 211 (4), 331–338. https://doi.org/10.1243/0957650971537231.

Otero, R., Gustavo, J., Patel, A., Diez S, R., Pecnik, R., 2018. Turbulence modelling for flows with strong variations in thermo-physical properties. International Journal of Heat and Fluid Flow 73, 114–123. https://doi.org/10.1016/J.IJHEATFLUIDFLOW.2018.07.005.

Pham, H.S., Alpy, N., Ferrasse, J.H., Boutin, O., Tothill, M., Quenaut, J., Gastaldi, O., Cadiou, T., Saez, M., 2016. An approach for establishing the performance maps of the sc-CO2 compressor: Development and qualification by means of CFD simulations. International Journal of Heat and Fluid Flow 61, 379–394. https://doi.org/10.1016/J.IJHEATFLUIDFLOW.2016.05.017.

Pilavachi, P.A., 2002. Mini- and micro-gas turbines for combined heat and power. Applied Thermal Engineering 22 (18), 2003–2014. https://doi.org/10.1016/S1359-4311(02)00132-1.

Rusch, D., Casey, M., 2013. The design space boundaries for high flow capacity centrifugal compressors. Journal of Turbomachinery 135 (3). https://doi.org/10.1115/1.4007548.

SAE International, 2019. AIR1168/1: Thermodynamics of Incompressible and Compressible Fluid Flow. Technical Report.https://www.sae.org/standards/content/air1168/1/

Schiffmann, J., Favrat, D., 2009. Experimental investigation of a direct driven radial compressor for domestic heat pumps. International Journal of Refrigeration 32 (8), 1918–1928. https://doi.org/10.1016/j.ijrefrig.2009.07.006.

Schiffmann, J., Favrat, D., 2010. Design, experimental investigation and multi-objective optimization of a small-scale radial compressor for heat pump applications. Energy 35 (1), 436–450. https://doi.org/10.1016/j.energy.2009.10.010.

Senoo, Y., Kinoshita, Y., 1977. Influence of inlet flow conditions and geometries of centrifugal vaneless diffusers on critical flow angle for reverse flow. Journal of Fluids Engineering, Transactions of the ASME 99 (1), 98–102. https://doi.org/10.1115/1.3448577.

Stanitz, J., 1952. One-dimensional compressible flow in vaneless diffusers of radial-and mixed-flow centrifugal compressors, including effects of friction, heat transfer and area change. Technical Report.http://naca.central.cranfield.ac.uk/reports/1952/naca-tn-2610.pdf

Tiainen, J., Jaatinen-Värri, A., Grönman, A., Sallinen, P., Honkatukia, J., Hartikainen, T., 2021. Validation of the Axial Thrust Estimation Method for Radial Turbomachines. International Journal of Rotating Machinery 2021. https://doi.org/10.1155/2021/6669193.

Van den Braembussche, R., 2019. Design and Analysis of Centrifugal Compressors, 1st. Wiley.https://books.google.it/books?hl=it&lr=&id=hFt-DwAAQBAJ&oi=fnd&pg=PR11&dq=design+and+analysis+of+centrifugal&ots=OtvpM4BBxt&sig=kZzfWqil48NBU7lFQPXGf9CV8DY&redir_esc=y#v=onepage&q=designandanalysisofcentrifugal&f=false

Whitfield, A., Baines, N., 1990. Design of radial turbomachines. Longman.https://www.osti.gov/biblio/6550042

Zagarola, M.V., McCormick, J.A., 2006. High-capacity turbo-Brayton cryocoolers for space applications. Cryogenics 46 (2-3), 169–175. https://doi.org/10.1016/J.CRYOGENICS.2005.11.018.

Zwyssig, C., Kolar, J.W., Round, S.D., 2009. Megaspeed drive systems: Pushing beyond 1 million r/min. IEEE/ASME Transactions on Mechatronics 14 (5), 564–574. https://doi.org/10.1109/TMECH.2008.2009310.